Geophysical Journal International

Frequency-Difference Backprojection of Earthquakes

Journal:	*Geophysical Journal International*
Manuscript ID	Draft
Manuscript Type:	Research Paper
Date Submitted by the Author:	n/a
Complete List of Authors:	Neo, Jing Ci; University of Michigan, Earth and Environmental Science Fan, Wenyuan; University of California San Diego Scripps Institution of Oceanography, Huang, Yihe; University of Michigan, Earth and Environmental Sciences; University of Michigan–Ann Arbor Dowling, David; University of Michigan, Naval Architecture and Marine Engineering
Keywords:	Earthquake source observations < SEISMOLOGY, Time series analysis < GEOPHYSICAL METHODS, Computational seismology < SEISMOLOGY, Wave propagation < SEISMOLOGY, Body waves < SEISMOLOGY

Frequency-Difference Backprojection of Earthquakes

Jing Ci Neo[1], Wenyuan Fan[2], Yihe Huang[1], & David Dowling[3]

[1]Department of Earth and Environmental Sciences, University of Michigan, Ann Arbor, Michigan, United States

[2]Scripps Institution of Oceanography, UC San Diego, La Jolla, California, USA

[3]Department of Naval Architecture and Marine Engineering, University of Michigan, Ann Arbor, Michigan, United States

Corresponding author: Jing Ci Neo, `neoj@umich.edu`

Summary

Back-projection has proven useful in imaging large earthquake rupture processes. The method is generally robust and does not require many assumptions about the fault geometry or the Earth velocity model. It can be applied in both the time and frequency domain. However, back-projection images are often obtained from records filtered in a narrow frequency range, limiting our ability to uncover the whole rupture process. Here we develop and apply a novel frequency-difference backprojection (FDBP) technique to image large earthquakes, which imitates frequencies below the bandwidth of the signal. The new approach originates from frequency-difference beamforming, which was initially designed to locate acoustic sources. The method stacks the phase-difference of frequency pairs, given by the autoproduct, and is less affected by multipathing and structural inhomogeneities. Additionally, it can potentially allow us to locate sources more accurately even in the presence of strong near-source scattering, albeit with lower resolution. In this study, we first develop the FDBP algorithm and then validate it by performing synthetic tests. We further compare two different stacking techniques of the FDBP method and their effects in the back-projection images. We then apply both the FDBP and conventional time-domain back-projection methods to the 2015 M 7.8 Gorkha earthquake as a case study. The back-projection results from the two methods agree well with each other, and we find that the peak radiation loci have standard error of less than 0.2° through a bootstrapping test. The FDBP method shows promise in resolving complex earthquake rupture processes in tectonically complex regions.

Key words: Earthquake source observations; Time-series analysis; Computational seismology; Body waves; Wave propagation

1 INTRODUCTION

Understanding earthquake rupture processes is fundamental to studying earthquake physics and estimating seismic hazards. However, large earthquakes often rupture in complex ways, which are challenging to resolve via traditional means. Backprojection is an imaging technique to study earthquake rupture evolution [*Ishii et al.*, 2005; *Krüger and Ohrnberger*, 2005]. The method is data driven but computationally efficient; thus, it has potential in hazard warning applications [e.g., *Hayes et al.*, 2011]. Uniquely, backprojection can take advantage of coherent high-frequency seismic body waves to discern earthquake rupture velocity and slip extent without assuming a fault geometry [see summary in *Kiser and Ishii*, 2017]. Hence, backprojection results have led to improved understanding of the inter-relations between rupture propagation, fault geometry, surrounding material lithology, and earthquake triggering [*Walker and Shearer*, 2009; *Meng et al.*, 2012a; *Fan et al.*, 2017, 2019].

Backprojection uses simple *P* waves and takes advantage of source-receiver reciprocity to image earthquakes. The method can be implemented in either the time domain or the frequency domain [e.g., *Manchee and Weichert*, 1968; *Goldstein and Archuleta*, 1987; *Ishii et al.*, 2005; *Krüger and Ohrnberger*, 2005; *Tan et al.*, 2019], and it has also been applied to various arrays with different configurations [e.g., *Xu et al.*, 2009a; *Kiser and Ishii*, 2012; *Wang and Mori*, 2011]. Although the data processing procedures of different methods can cause some variations [*Rost and Thomas*, 2002; *Meng et al.*, 2016; *Qin and Yao*, 2017], the general rupture features are similar [*Zhang et al.*, 2016; *Yagi and Okuwaki*, 2015; *Liu et al.*, 2017; *Wang and Mori*, 2016; *Avouac et al.*, 2015], showing the robustness of the backprojection results. The stability results from stacking coherent waveforms, and the approach does not perform a formal inversion with physical constraints. However, the method can suffer from imaging artifacts when there are coherent signals that are not due to the rupture process [e.g., *Meng et al.*, 2012b]. Such artifacts can be caused by near-source scatters, e.g., depth phases and water phases [*Yue et al.*, 2017; *Fan and Shearer*, 2018]. The backprojection images can also suffer from strong 3D velocity influences in causing inaccurate travel time predictions or limited array footprints that can distort the array responses [e.g., *Okuwaki et al.*, 2014; *Meng et al.*, 2016]. Furthermore, complex ruptures may involve multiple distinct faults that have varying focal mechanisms, posing challenges to accurately resolve the spatiotemporal propagation of these earthquakes [e.g., *Zeng et al.*, 2020]. Mitigating these biases and quantifying the solution uncertainties remain key issues in backprojection studies.

Here, we develop a novel frequency-difference backprojection method (FDBP) aimed to address the uncertainties in earthquake imaging. The frequency-difference method was first introduced in acoustics beamforming [*Abadi et al.*, 2012]. It can accurately resolve the arrival of a signal even in the presence of wave propagation effects that cannot be fully characterised by a known velocity model. The basis of this method lies in the inherent tradeoff between robustness and resolving power of any given wavelength. Backprojection of higher frequencies becomes increasingly unstable as the period of the waves approaches the magnitude of error in predicted travel times. To circumvent this limitation, the frequency-difference method uses "autoproducts" to simulate lower frequencies. The autoproduct is given by the quadratic product of a complex wavefield with the complex conjugate of another wavefield at a different frequency. The phase-difference of each frequency pair mimics the phase of a wave at the difference-frequency (Figure 1). Such a procedure can potentially resolve source locations with higher accuracy (Figure 1B), albeit with lower resolution. Additionally, the autoproducts can be averaged incoherently over a frequency band of interest, which may further reduce the error from multipathing or scattering under certain conditions [*Worthmann and Dowling*, 2017]. We elaborate on the theory of FDBP in Section 2.

In this study, we first develop the theoretical and numerical frameworks of using FDBP to image earthquakes, and then apply the method to the 2015 Mw 7.8 Gorkha, Nepal earthquake to investigate its rupture process as a case study. We evaluate the method by performing synthetic tests using both Ricker and real seismic waveforms. Our synthetic tests are benchmarked with results from a conventional time domain backprojection method. We also explore a range of empirical parameters used in the FDBP imaging procedure to examine the effects of the parameter choices. In general, FDBP can image seismic radiation accurately and appears less sensitive to the noise level when compared to conventional backprojection methods. For the 2015 Gorkha earthquake, the rupture characteristics resolved by FDBP are consistent with previous results, especially in a high frequency (0.3-2Hz) band. Our results show that FDBP is a promising new method, and its robust results may provide new insights into complex earthquake rupture processes.

2 THEORY

2.1 Conventional Backprojection

Conventional time-domain *P*-wave backprojection aligns the seismic waveforms with their initial arrivals, and then back-propagates the records to a set of grid points near the earthquake hypocenter to infer its rupture process. For simplicity, herein the conventional time-domain back-projection is referred as CTBP to compare with FDBP. The stacked waveforms from CTBP at a candidate source (grid location $\underline{r}$) is given by

$$B_{\text{conv}}(\underline{r},t) = \sum_{k=1}^{N} \frac{1}{n_k} d_k(t - \tau_k(\underline{r}) - s_k) \tag{1}$$

where $d_k(t)$ is the velocity record of the k^{th} station at time t, $\underline{r}$ is the source grid location, $\tau_k(\underline{r})$ is the predicted travel time from $\underline{r}$ to the k^{th} station, and s_k is the time correction term obtained from cross-correlation (Section 3.1). The velocity record of each station is inversely weighted by the total number of stations within 5 degrees of the station, n_k, to enhance the signals recorded at sparsely distributed stations [e.g., *Fan et al.*, 2016]. Finally, the backprojection energy is computed as the root-mean-square of the stacked waveforms over a time window T:

$$E_{\text{conv}}(\underline{r}) = \sqrt{\langle (B_{\text{conv}}(\underline{r},t))^2 \rangle_T} \tag{2}$$

In the frequency domain, conventional backprojection shifts the spectra in phase, stacks spectra from different stations, and averages the stacks over the frequency band of interest. The phase-shifts are equivalent to the time-shifts in the time domain. The waveforms are divided into segments to investigate the temporal propagation. Taking the earthquake hypocenter as a reference point ($\underline{r}^0$) for the first time window, the time-shift at grid $\underline{r}$ can be rearranged as

$$\begin{aligned} \tau_k(\underline{r}) &= \tau_k(\underline{r}^0) + [\tau_k(\underline{r}) - \tau_k(\underline{r}^0)] \\ &= \tau_k(\underline{r}^0) + \Delta\tau_k^0(\underline{r}) \end{aligned} \tag{3}$$

where $\tau_k(\underline{r}^0)$ determines the onset of the time window segments and $\Delta\tau_k(\underline{r})$ is used in the phase-shift of the waveforms to obtain the back-projection images. As the rupture moves away from the hypocenter, a Doppler correction is needed to ensure that seismic phases from the same slip episode are included in one time window. Hence, we use the peak energy location of the previous time window as the reference point for the successive time window [e.g., *Meng et al.*, 2012b; *Wang et al.*, 2016; *Yin et al.*, 2018]. This method works best for simple rupture cases, such as unilateral, continuous rupture propagations.

Taking $P_k(\omega)$ as the spectrum of the k^{th} station for a time window, where ω is the frequency, the backprojection result at frequency ω is

$$B_{\text{conv}}(\underline{r},\omega) = \left| \sum_{k=1}^{N} \frac{1}{n_k} P_k(\omega) w_k(\underline{r},\omega) \right|^2 \tag{4}$$

where $w_k(\underline{r},\omega) = e^{i\omega\Delta\tau_k^0(\underline{r})}$ is a phase-weighting factor, and the backprojection energy is then calculated by averaging over the frequency range of interest.

$$E_{\text{conv}} = \left\langle B_{\text{conv}}(\underline{r},\omega) \right\rangle_\omega \tag{5}$$

2.2 Frequency-Difference Backprojection

When applying the frequency-difference backprojection (FDBP), the complex wavefield term in Equation 5 is substituted with the autoproduct, the product of complex wavefields [*Douglass and Dowling*, 2019]. The autoproduct simulates a wave at the difference-frequency using the phase difference of a pair of frequencies (Figure 1A). Assuming that the phase of the source is approximately constant over the frequency band of interest [*Worthmann and Dowling*, 2017] and that arrivals of lower frequency seismic waves can be better predicted, backprojecting the autoproduct decreases the impact of travel time error on the accuracy of the phase shift (Figure 1B). The autoproduct, AP_k, measured at the k^{th} station for a pair of frequencies, is defined as:

$$AP_k(\bar{\omega}, \Delta\omega) = P_k(\omega_2)P_k^*(\omega_1) = P_k\left(\bar{\omega} + \frac{\Delta\omega}{2}\right)P_k^*\left(\bar{\omega} - \frac{\Delta\omega}{2}\right) \quad (6)$$

where $\bar{\omega}$ is the average and $\Delta\omega$ is the difference of two frequencies, ω_1 and ω_2.

The autoproduct can then be averaged incoherently (BWAP – Band Width Averaged Autoproduct) or coherently (non-BWAP) over the frequency pairs. Here, averaging incoherently (BWAP) means averaging the spectra of the available frequency pairs (complex value) before stacking. Averaging coherently (non-BWAP) means averaging the backprojection results of each pair (real value) after stacking. The incoherently averaged (BWAP) autoproduct is defined as

$$\overline{AP}_k = \langle AP_k(\bar{\omega}, \Delta\omega)\rangle_\omega = \frac{1}{M}\sum_{m=1}^{M} AP_k(\bar{\omega}_m, \Delta\omega) \quad (7)$$

for M sets of average frequencies.

The BWAP procedure can improve the robustness of the results in the presence of random noise and signal-generated noise in earthquake P waves by suppressing additional terms due to the multiple path effects, e.g., scattered or reflected waves from multiple ray paths [*Worthmann et al.*, 2017; *Douglass et al.*, 2017]. It is most effective if the frequency range (bandwidth) is sufficiently wide such that there are enough averaging pairs. The required bandwidth depends on the time difference between the interfering ray paths, and is given by the condition $(\Delta\Omega_{H-L} - \Delta\omega)|\Delta\tau_{m-l}| >= 2\pi$ [*Worthmann and Dowling*, 2017], where $\Delta\Omega_{H-L}$ is the averaging bandwidth, $\Delta\omega$ is the difference-frequency, and $\Delta\tau_{m-l}$ is the arrival time differences of two ray paths. For example, this condition is satisfied for difference-frequencies of 0.1 Hz when the signal bandwidth is ≥1.7 Hz for arrival-time differences of 4s or longer. Hence, the smaller the value of $\Delta\omega$, the more robust BWAP is to random noise and reflected waves.

The FDBP outputs for both averaging methods at a difference-frequency, $\Delta\omega$, are given by

$$B_{\Delta,\mathrm{BWAP}}(\underline{r}, \Delta\omega) = \left| \sum_{k=1}^{N} \overline{AP}_k(\Delta\omega) w_k(\underline{r}, \Delta\omega) \right|^2 \tag{8}$$

and

$$B_{\Delta,\mathrm{non-BWAP}}(\underline{r}, \Delta\omega) = \left\langle \left| \sum_{k=1}^{N} AP_k(\bar{\omega}, \Delta\omega) w_k(\underline{r}, \Delta\omega) \right|^2 \right\rangle_{\omega} \tag{9}$$

The final backprojection results can be obtained by averaging over a range of difference-frequency pairs to increase the robustness of the results [*Douglass et al.*, 2017]. The output of FDBP in this study is defined as

$$B_{\Delta}(\underline{r}) = \left\langle B_{\Delta}(\underline{r}, \bar{\omega}) \right\rangle_{\Delta\omega} \tag{10}$$

which varies for different stacking time windows and can be used to track earthquake rupture propagation.

3 DATA AND METHODS

In this section, we describe the data processing steps for synthetic and real waveforms as well as the practical implementations of CTBP and FDBP for the synthetic cases and the 2015 Mw 7.8 Gorkha earthquake. To benchmark our FDBP mainshock results with the images obtained from CTBP, we designed two sets of resolution and uncertainty analyses using both synthetic and observed seismograms. We also bootstrap the records to statistically analyze the result sensitivity to the global array configuration.

3.1 Seismic Data Selection and Processing

For synthetic seismograms, we use the Ricker wavelet to approximate *P*-wave pulses (Figure 3A). The Ricker wavelet has a constant phase over 0.3–2 Hz. The constant phase simplifies the implementation of BWAP [*Worthmann and Dowling*, 2017], and such an exercise helps to isolate the effects of inaccurate travel times in the backprojection images. A single Ricker wavelet [*Ricker*, 1953] in the time domain is defined as

$$d_{\mathrm{Ricker}}(t) = \left(1 - \frac{1}{2}(2\pi f_p)^2 t^2\right) \exp\left(-\frac{1}{4}(2\pi f_p)^2 t^2\right) \tag{11}$$

where f_p is the peak frequency (Hz) and t denotes time. In this study, the peak frequency f_p is 1 Hz. For a multiple source case, synthetic seismograms of each source are generated independently and then summed together at each station.

We download globally distributed, vertical-component, broadband *P*-wave records from the Data Management Center of the Incorporated Research Institutions for Seismology (see Data Availability), including records of Mw 6.6 (2015/04/25) and Mw 6.7 (2015/04/26) aftershocks, and those of the 2015 Mw 7.8 Gorkha earthquake. The records are processed in a similar manner. The stations are within 30° to 90° epicentral distance from the respective hypocenters. In total, we use 155 unique stations to image the 2015 Gorkha mainshock and 45 stations for the aftershock test. To compare our Mw 7.8 Gorkha earthquake results to other studies, we evaluate the seismograms in two frequency bands, 0.05–0.5Hz (low frequency, LF, Figure 2B) and 0.3–2Hz (high frequency, HF, Figure 2C). The seismograms are filtered with a zero-phase 4th order Butterworth filter. For each frequency band, the filtered records with signal-to-noise ratios (SNR) less than 3 are discarded. The SNR is defined as the root-mean-square (RMS) amplitude ratio from time windows 10 s before and 10 s after the theoretical *P*-wave arrival obtained from IASP91 [*Kennett and Engdahl*, 1991]. To balance the station distribution, we group stations into one-degree azimuthal bins and only select one record per bin in each cluster. Finally, the records are visually examined, and we only keep the ones that have clear, simple *P*-wave onsets.

To reduce impacts from three-dimensional (3D) Earth velocity structures, we empirically correct possible travel time errors by aligning the waveforms before the backprojection analyses. The waveforms are aligned using a multichannel cross-correlation method for the two frequency bands independently [*VanDecar and Crosson*, 1990; *Shearer*, 1997; *Hauksson and Shearer*, 2005]. In this method, we construct linear inverse problems using the differential times obtained from pairwise cross-correlations, weighting each pair by their cross-correlation coefficients. The optimal set of values (time correction) minimizes the ℓ_1 misfit, and are calculated using the CVX package [a package for solving convex problems, *Grant and Boyd*, 2008]. The final optimal time corrections are obtained after iteratively repeating this inversion procedure using different window lengths, where subsequent iterations of alignment are based upon the previous corrections. Low-frequency records are aligned after two iterations using time windows of -8–8 s and 0–6 s relative to the theoretical *P*-wave arrival. High-frequency records are aligned after three iterations, using time windows of 1.5–8 s, 0–6 s, and 0.6–1.7 s. In addition, the HF timeshifts of stations NWAO and KOM are manually corrected. These windows are visually selected to align the waveforms using the earliest strong pulses.

We generate composite seismograms as "synthetic" data by summing real seismic records of the Mw 6.6 and Mw 6.7 aftershocks. The two earthquakes have similar focal mechanisms to that of the mainshock. The first aftershock locates close to the mainshock epicenter while the second aftershock situates near the eastern end of the slip distribution (Figure 2). The records are first filtered at 0.3–2 Hz, and normalized by the first 5 s from their arrival times. These waveforms of the two events recorded by the same station are then scaled by a set of amplitude ratios and summed together from 40 s before to 60 s after their predicted *P* wave arrivals from the two events with a 20 s delay for the second event. We adopt the same set of empirical time corrections obtained for the Mw 6.6 earthquake for later analyses. The time corrections are different for the two earthquakes at the same station. This is likely due to the near-source small-scale 3D velocity structures. Hence, applying backprojection analyses to the composite "synthetic" data will allow us to examine the realistic effects of multiple paths, reflections, and noise.

3.2 Backprojection Analyses

We apply CTBP and FDBP methods to both synthetic and observed seismograms to compare their performance. The waveforms are processed in the same way for the two analyses. The waveforms are self-normalized by the maximum amplitude of the first few seconds of the *P* waves to remove effects from site conditions, radiation pattern, and instrument gains. The normalizing window is set as 10 s for the synthetic seismograms, 5 s for the composite records, and 20 s for the 2015 Gorka mainshock. To locate potential sources, we set source grids of 400 by 400 km with a 5 km spacing covering an area of 26.4°–30.0° and 82.8°–86.9° in latitude and longitude. The grids are fixed at the hypocentral depth of 10 km. The same set of potential source grids are used for all the analyses in this study, including the uncertainty analyses. Theoretical *P*-wave travel times of the grids are computed using the IASP91 velocity model [*Kennett and Engdahl*, 1991].

For CTBP, we apply the *N*th root stacking approach to sharpen the images and reduce the noise influence at the cost of absolute amplitude information [*McFadden et al.*, 1986]. The nonlinear stacking strategy has been successfully implemented in backprojection analyses, and we use $N = 4$, which has yielded well-resolved results [e.g., *Xu et al.*, 2009b]. Evolution of the rupture process can be inferred from the snapshots of the backprojection energy bursts. Here we use a snapshot window length of 10 s with a 10 s time step starting from -5 s.

For FDBP, we use the same start time and time steps but longer time windows of 15 s duration to increase frequency resolution. The range of difference-frequencies used directly impact the FDBP results. We empirically select the difference frequency ranges by trial-and-error tests as 0.05-0.15 Hz for the Ricker test and 0.05–1.5 Hz for the aftershock tests. For the mainshock analysis, we used 0.07–0.33 Hz for LF BWAP, 0.07–0.4 Hz for LF non-BWAP, 0.13–0.47 Hz for HF BWAP and 0.33–1.27 Hz for the HF non-BWAP. We use a reference point time-windowing strategy for FDBP as detailed in Section 2 to ensure that coherent phases recorded by all stations can be used to image rupture propagation for the same time windows. The theoretical travel time $\tau_k(\underline{r}^{\text{ref}})$ from the peak location of the previous time window is used to determine the onsets of the following time windows of the stations.

3.3 Uncertainty Analyses

We use the Ricker wavelet synthetic seismograms to assess the FDBP robustness against the travel time error. We use the Mw 6.6 and Mw 6.7 aftershock locations to compute the synthetic seismograms, assuming a 20 s time separation between the two sources, and apply both CTBP and FDBP to the synthetic seismograms to resolve the two sources. The stations are randomly placed within an epicentral distance range of 30° to 90° from the location of the first source (Figure 3A). The station distances are drawn from a normal distribution with a mean of 60° and standard deviation of 12°, while the azimuthal distribution is drawn from a uniform distribution from 0° to 360°. Synthetic seismograms are computed at these stations as the superpositions of the Ricker wavelet functions (Equation 11), and then filtered at 0.3–2 Hz. To simulate the travel time error, we add a random arrival time perturbation to the synthetic seismograms for the second source. The random perturbation are drawn from a zero mean normal distribution with a standard deviation of 2 s, which is likely greater than the observed travel time errors.

To evaluate the effects of signal-generated noise, we apply the CTBP and FDBP imaging procedures to the composite "synthetic" data. The synthetic Ricker wavelet test is useful to isolate the impacts of potential travel time errors. However, the simple waveforms do not reassemble the real observations, which often contain coda waves and noises. Here, the noise arises from random sources or structural scatterers. Such noise contributions are coherent and may cause artifacts that are difficult to distinguish from true rupture features. Hence, we create a second synthetic test using real waveforms and apply the CTBP and FDBP imaging methods following the procedure described in Section 3.2. The imaging results of the second source depend on the amplitude ratio between the P-waves of the two earthquakes, and we discuss the effects of this ratio in the following section.

For the mainshock case study, we statistically examine the results by bootstrapping the stations. Specifically, we randomly re-sample the stations following a uniform distribution to obtain an array with the same number of stations, and repeat the CTBP and FDBP backprojection analyses for 1000 times, respectively. We quantify the image uncertainties as the standard errors of the latitude and longitude of peak energy locations. Lastly, we calculate the normalized peak power time functions for both FDBP averaging approaches using the same difference-frequency ranges as the results in Figure 4, and compare them to the normalized moment rate function of the finite-fault model in *Galetzka et al.* [2015]. The normalized peak power time functions for FDBP are calculated using a time window of 15 s duration and an increment time step of 1 s. The normalized moment rate function of *Galetzka et al.* [2015] is calculated with non-overlapping 1 s windows.

4 RESULTS

4.1 Resolution and Uncertainty

As described in Section 1, there are intrinsic ambiguities in backprojection images. To understand the resolution and uncertainty of our results, we evaluate the FDBP method using a set of synthetic tests before comparing the mainshock results to previous studies. We first apply the imaging procedures outlined in Section 3.2 to the Ricker wavelet synthetic seismograms. To make a quantitative evaluation of the results, we examine the distances between the peak energy loci and the input source locations to assess the accuracy of the results. Figure 3A–D show the setup and results of a test run. We find that both the FDBP and CTBP methods can resolve the synthetic sources well. In the FDBP framework, the BWAP and non-BWAP procedures produce similar results with a standard error of 0.03°, while CTBP results have a standard error of 0.22° (Figure 3B–D). We also observe that using lower values of difference-frequencies leads to more accurate results but at lower resolutions. These results validate our numerical implementation of FDBP.

Similarly, we apply both backprojection methods to the composite "synthetic" seismic records from the Mw 6.6 and Mw 6.7 aftershocks. We implement the same procedures as applied to the synthetic tests and use the same set of parameters as detailed in Section 3.2. The composite records include pre-*P*-wave noises and *P*-wave coda waves of the two earthquakes. The coda wave from the first source overlaps with the arrival of the second source, and the resolvability of the second source strongly depends on the relative *P*-wave amplitudes. When the amplitude ratio of the first source to the second source is 2, the FDBP method can locate the second source using either of the averaging approaches (BWAP or non-BWAP), while CTBP fails to do so in this test (Figure 3E–G). Additionally, both BWAP and non-BWAP work well for a large range of difference-frequencies. This shows that for transient seismic sources, BWAP is a feasible method as long as we stack over a wide range of frequencies for the given time windows. In summary, the synthetic tests show that FDBP has a potential advantage over CTBP when the records are noisy and may be better suited to image later rupture stages of large earthquakes when seismic radiations are likely obscured by coda waves.

4.2 Backprojection images of the 2015 Mw 7.8 Gorkha earthquake

We image the 2015 MW 7.8 Gorkha earthquake with both the CTBP and FDBP (BWAP and non-BWAP) methods in two frequency bands (0.05–0.5 Hz, LF and 0.3–2 Hz, HF, Figure 4). The conventional time domain approach yields similar results as reported by previous studies [e.g., *Fan and Shearer*, 2015; *Avouac et al.*, 2015]. Here we focus on the FDBP results and highlight the new features. We find that both the BWAP and non-BWAP results can capture the general rupture process of the 2015 Mw 7.8 Gorkha earthquake (Figure 5B,C), but with some variation in the details of the snapshots.

First, we examine the FDBP BWAP results. The LF BWAP snapshot results (Figure 4B) show three distinct rupture stages: a slow initial stage for the first 10 seconds, a steady propagation stage from 20 to 40 s, and a final termination stage for the last 10 seconds. The initial stage features a slow rupture development with an apparent rupture speed that is almost stationary (Figure 5E). The initial stage is manifested in the first 10 s waveforms that show little moveout (Figure 2C). The earthquake rupture then propagated in a curved line towards the southeast direction in the second stage and halted before reaching the May 12 Mw 7.3 aftershock. Finally, the backprojection images suggest a somewhat chaotic termination stage, showing an apparent rupture episode towards the updip direction (shallower depth). The LF BWAP snapshot results share similar features to those from the LF CTBP method, but the peak energy loci during 30–35s seem to be located at deeper depths (Figure 5D,E). The HF BWAP snapshots (Figure 4E) are slightly different from the LF BWAP ones. They appear to cluster around three distinct locations – the hypocenter, the peak slip location of the earthquake, and the point where the rupture transitions towards the updip direction in the last stage. Additionally, the cluster around the peak slip is located further up-dip compared to the corresponding LF BWAP snapshots.

Both the LF and HF non-BWAP results also suggest that the earthquake rupture is almost stationary for the first 10 s, but there are some variations in the later-stage non-BWAP results compared to those of BWAP. From 10 to 55 s, the non-BWAP results show that the rupture propagates continuously in a linear fashion, different from the BWAP or CTBP results. Further, the HF non-BWAP results do not suggest an abrupt up-dip rupture transition in the last stage but a northwest rupture before the earthquake termination. Loci of the LF non-BWAP snapshots are also located further down-dip compared to their HF snapshots or the CTBP images. In general, we find that the BWAP and non-BWAP FDBP peak loci are located within the 1 m slip contours of the *Wang and*

Fialko [2015] and *Galetzka et al.* [2015] finite-fault slip models (Figure 5B and D), and the LF loci tend to trace the downdip edge of the slip.

The BWAP and non-BWAP results depend on the frequency range of the difference-frequency. For example, lower values of difference-frequencies would lead to more coherent BWAP images, as theorized in Section 2. The non-BWAP stacking approach appears to be able to utilize a larger range of difference-frequencies, but the results may vary when using different difference-frequencies. For example, using a bandwidth of 0.13-0.87 Hz would result in similar non-BWAP images as to the HF BWAP snapshots.

The location uncertainties (standard error of the peak locations) from the bootstrapping analysis are visualized as error bars in Figure 4, representing the sensitivity of each method to the global array station distribution. Lower standard deviations do not necessarily mean that the results are more accurate as the bootstrapping procedure only tests the sensitivity of the results to the station distribution. In general, the location uncertainty increases as the rupture progresses, which is likely due to interference from coda waves or travel time error from near-source heterogeneities. The CTBP results have small location standard deviations comparing to the FDBP results. We also observe that the LF CTBP results have greater latitude uncertainties than those of the HF CTBP results. The LF and HF BWAP features have similar uncertainties, while the LF non-BWAP results have lower uncertainties than those of the HF non-BWAP results. The greater standard deviations of the HF non-BWAP locations may result from the broader difference-frequency range, which helps to enhance the resolution but compromises the robustness.

Lastly, we find that the normalized peak power time functions and the normalized moment rate function from *Galetzka et al.* [2015] share similar patterns (Figure 5A and C) with an exception of the 24–34 s HF BWAP results. Back-projection normalized peak power time functions often have different patterns compared to the finite-fault moment rate functions, and our results show that FDBP might help to connect high-frequency seismic radiation to lower frequency seismic slip. We find that the LF and HF peak power time functions are more similar for non-BWAP than BWAP. The FDBP normalized peak power time functions also tend to have relatively higher values at around 40 s than the normalized moment rate function of *Galetzka et al.* [2015].

5 DISCUSSION

The mainshock rupture features are imaged consistently using the CTBP and FDBP methods in the high frequency band (0.3–2 Hz), including the three main rupture stages as described in

Section 4.2. These features are also reported in previous backprojection and finite-fault inversion studies [e.g., *Fan and Shearer*, 2015; *Grandin et al.*, 2015; *Wang and Mori*, 2016; *Yagi and Okuwaki*, 2015; *Avouac et al.*, 2015; *Galetzka et al.*, 2015], confirming the robustness of our results. The general good agreement between the CTBP and FDBP images supports the feasibility of the FDBP method. Additionally, the location uncertainties in the CTBP and LF non-BWAP results are low, with most loci standard errors less than 0.2°. These results suggest that the FDBP images are robust. Furthermore, the HF results are obtained from using globally distributed seismic records filtered up to 2 Hz frequency content, which is a significant increase of the commonly used frequency band in previous global backprojection studies [e.g., *Walker and Shearer*, 2009; *Fan and Shearer*, 2016].

Details of the CTBP and FDBP snapshots of the 2015 Gorkha earthquake differ from each other for a few time windows. For example, the peak CTBP radiation around 35 s is located updip near Kathmandu, but this is not observed in the FDBP results. To investigate the possible cause, we realigned the LF waveforms at time window 8 (centered at 35 s) based on the peak loci of the CTBP and FDBP non-BWAP results (Figure 6). The waveforms appear to be more coherently aligned using the FDBP loci compared to CTBP.

The observed differences can be caused by the different windowing approaches of CTBP and FDBP. Each potential grid point is treated independently in CTBP, and the continuous stacked-wavetrains at each point can naturally resolve the rupture propagation when compared among the set of grids. In contrast, FDBP employs the reference-window strategy (Section 2) to track down the rupture process. Therefore, the final CTBP images are obtained from different *P*-wave windows for the grid points in a given snapshot, whereas FDBP uses the same time window for all grid points. It suggests that possibly mismatched *P*-wave pulses are more likely to be included in the same CTBP stacking window than that of FDBP, causing spatially clustered snapshots. On the other hand, the reference-window strategy may have resulted in larger bootstrap uncertainties for the FDBP results. This is because the reference points in FDBP are different for each time window, and any difference in the initial snapshots can be amplified for subsequent snapshots, resulting in greater location uncertainties.

The differences in the CTBP and FDBP results could have also arisen from the differences in measuring coherence. CTBP stacks the waveforms in the time domain, and amplitudes of the pulses strongly impact the final results. FDBP stacks the phase-difference of frequency pairs in the frequency domain, and the coherence of the pairs determines the images. In comparison, CTBP results are more likely influenced by the amplitudes of the waveforms, while FDBP results would be more sensitive to the shape of the pulses. The Gorkha earthquake ruptured unilaterally, showing a strong rupture directivity effect, which caused the relative amplitudes of each pulse to vary between stations. Consequentially, the CTBP images may have been impacted to generate sporadic radiation clusters, while the FDBP snapshots suggest a more continuous rupture propagation.

Travel-time error, interference from depth phases, noise at individual stations, variations in focal mechanism, and the frequency-dependent seismic radiation of large earthquakes could have impacted the CTBP and FDBP results as well. For example, FDBP simulates lower, out-of-band frequencies by using autoproducts, which makes the method less sensitive to travel-time error. Moreover, FDBP is less affected by interferences from noise or reflected waves. FDBP may also mitigate the impact of variations in focal mechanism during earthquake ruptures, as the phase-differences of frequency pairs are not affected by polarity flips. The details of these effects remain open questions and require further analysis using both synthetic and real data. One future direction involves the application of FDBP and CTBP to image simulated dynamic rupture scenarios to explore and quantify the possible imaging uncertainties.

We find that the two averaging approaches, BWAP and non-BWAP, appear to have different impacts in different implementations. For example, both averaging approaches perform equally well for our synthetic tests (Figure 3). However, for the 2015 Gorkha mainshock, the non-BWAP results have lower location uncertainties and suggest a continuous, linear rupture propagation, slightly different from those of the BWAP results (Figure 4). In contrast, previous acoustic studies find that BWAP is superior at locating sources than non-BWAP [*Douglass et al.*, 2017]. The variations in performances may be from the complexities in the source characteristics and the wave propagations — the acoustic experiments have an idealized laboratory experiment setup; the aftershock synthetic tests use simple point sources, and the Gorkha mainshock ruptured over 160 km [*Galetzka et al.*, 2015]. In the acoustic experiments, the sources are static and emit Gaussian-windowed chirp pressure waves with frequencies over a hundred of kilohertz [*Lipa et al.*, 2018]. The media (water) is homogeneous, and the boundary conditions are given. On the other hand, large earthquakes can rupture over hundreds to thousands of kilometers and radiate seismic waves in complex ways [*Ishii et al.*, 2005; *Lay et al.*, 2005]. The seismic array configuration is also less ideal than acoustic experiments, and the 3D Earth structure can cause complex P-wave field at higher frequencies. In general, it is difficult to directly compare laboratory results with field studies, and we caution direct comparisons of images of different sources and cases. A careful evaluation of the image uncertainties and a through examination of the parameters are necessary before interpreting the FDBP results.

However, it is remarkable that FDBP can be successfully used to image earthquake rupture processes despite the great differences.

FDBP is a promising new method and is still in an early stage of development. Here the imaging parameters are selected empirically to enhance the results of the 2015 Nepal earthquakes. These parameters are likely case-dependent for different earthquakes, and their effects on the FDBP results are yet to be explored. For example, the optimal difference-frequency range likely depends on the earthquake magnitude and its rupture process, e.g., length and duration, as well as the magnitude of the travel time errors and the reflected waves. The implementation of a global array allows the FDBP method to be used to image more earthquakes with good azimuthal coverage, although the waveforms may be less coherent for complex cases, requiring careful analyses to assure image robustness.

We find that both CTBP and FDBP can be effective in imaging earthquake rupture processes, and they both have unique merits in resolving different potential rupture features. Imaging earthquake with both methods and collectively analyzing earthquake rupture processes would potentially improve the understanding of rupture propagation details. Our Gorkha earthquake analysis shows that FDBP can provide an accurate, first-order estimate of the rupture energy and locations which could be useful for informing earthquake or tsunami rapid response efforts. Our synthetic tests show that FDBP has the potential to improve the accuracy of backprojection results, which would be particularly useful for resolving large earthquake rupture processes in structurally complex regions. It is possible to apply FDBP to moderate magnitude earthquakes using regional arrays and high frequency seismic records. Such events can be challenging to resolve using conventional approaches, and averaging over a large range of frequency pairs may enable the FDBP method to obtain reliable models that could advance our understanding of earthquake rupture processes.

6 CONCLUSION

We have developed a novel frequency-difference backprojection (FDBP) approach in the frequency domain that uses difference frequencies and autoproducts to image earthquake rupture processes. We further explore two different stacking strategies, BWAP and non-BWAP, which stack the spectra incoherently and coherently. The FDBP method has potential in reducing seismic radiation location uncertainty. From systematic uncertainty quantification exercises, we find that FDBP can reduce the impacts of inaccurate travel time errors as well as coda wave interference. We successfully apply FDBP to image the 2015 Gorkha Mw 7.8 earthquake in two frequency bands, and its main rupture features are robustly resolved. The FDBP results resemble those of conventional backprojection methods, and the obtained peak radiation loci have less than 0.2° standard deviations in general. Furthermore, we find that FDBP results depend on windowing strategies and parameter choices, such as difference-frequency ranges. The two stacking approaches reveal different details of the Gorkha earthquake rupture process, and the non-BWAP images suggest a continuous, linear rupture process. The FDBP method shows promise in resolving complex earthquake rupture processes in tectonically complex regions and can potentially be applied to image moderate magnitude earthquake rupture using regional arrays and high frequency seismic records.

ACKNOWLEDGEMENTS

J. C. Neo and Y. Huang acknowledge funding from the NSF grant EAR-1943742. W. Fan acknowledges funding from NSF grant EAR-2022441. We are grateful to Dr. Diego Melgar and Dr. Kang Wang for sharing their finite-fault slip models, and Dr. Jeroen Ritsema for his helpful comments and suggestions.

Data availability

The seismic data were provided by Data Management Center (DMC) of the Incorporated Research Institutions for Seismology (IRIS). The facilities of IRIS Data Services, and specifically the IRIS Data Management Center, were used for access to waveforms, related metadata, and/or derived products used in this study. IRIS Data Services are funded through the Seismological Facilities for the Advancement of Geoscience and EarthScope (SAGE) Proposal of the National Science Foundation (NSF) under Cooperative Agreement EAR-1261681.

References

Abadi, S. H., H. C. Song, and D. R. Dowling (2012), Broadband sparse-array blind deconvolution using frequency-difference beamforming, *The Journal of the Acoustical Society of America*, *132*(5), 3018–3029.

Avouac, J.-P., L. Meng, S. Wei, T. Wang, and J.-P. Ampuero (2015), Lower edge of locked Main Himalayan Thrust unzipped by the 2015 Gorkha earthquake, *Nature Geoscience*, *8*(9), 708–711.

Douglass, A. S., and D. R. Dowling (2019), Frequency-difference beamforming in the presence of strong random scattering, *The Journal of the Acoustical Society of America*, *146*(1), 122–134.

Douglass, A. S., H. Song, and D. R. Dowling (2017), Performance comparisons of frequency-difference and conventional beamforming, *The Journal of the Acoustical Society of America*, *142*(3), 1663–1673.

Fan, W., and P. M. Shearer (2015), Detailed rupture imaging of the 25 April 2015 Nepal earthquake using teleseismic P waves, *Geophysical Research Letters*, *42*(14), 5744–5752.

Fan, W., and P. M. Shearer (2016), Local near instantaneously dynamically triggered aftershocks of large earthquakes, *Science*, *353*(6304), 1133–1136, doi:10.1126/science.aag0013.

Fan, W., and P. M. Shearer (2018), Coherent seismic arrivals in the P wave coda of the 2012 Mw 7.2 Sumatra earthquake: Water reverberations or an early aftershock?, *Journal of Geophysical Research: Solid Earth*, *123*(4), 3147–3159.

Fan, W., P. M. Shearer, C. Ji, and D. Bassett (2016), Multiple branching rupture of the 2009 Tonga-Samoa earthquake, *Journal of Geophysical Research: Solid Earth*, *121*(8), 5809–5827.

Fan, W., D. Bassett, J. Jiang, P. M. Shearer, and C. Ji (2017), Rupture evolution of the 2006 Java tsunami earthquake and the possible role of splay faults, *Tectonophysics*, *721*, 143–150.

Fan, W., S. S. Wei, D. Tian, J. J. McGuire, and D. A. Wiens (2019), Complex and Diverse Rupture Processes of the 2018 M w 8.2 and M w 7.9 Tonga-Fiji Deep Earthquakes, *Geophysical Research Letters*, *46*(5), 2434–2448.

Galetzka, J., D. Melgar, J. F. Genrich, J. Geng, S. Owen, E. O. Lindsey, X. Xu, Y. Bock, J.-P. Avouac, L. B. Adhikari, et al. (2015), Slip pulse and resonance of the Kathmandu basin during the 2015 Gorkha earthquake, Nepal, *Science*, *349*(6252), 1091–1095.

Goldstein, P., and R. J. Archuleta (1987), Array analysis of seismic signals, *Geophysical Research Letters*, *14*(1), 13–16.

Grandin, R., M. Vallée, C. Satriano, R. Lacassin, Y. Klinger, M. Simoes, and L. Bollinger (2015), Rupture process of the Mw= 7.9 2015 Gorkha earthquake (Nepal): Insights into Himalayan megathrust segmentation, *Geophysical Research Letters*, *42*(20), 8373–8382.

Grant, M., and S. Boyd (2008), Graph implementations for nonsmooth convex programs, in *Recent Advances in Learning and Control*, edited by V. Blondel, S. Boyd, and H. Kimura, Lecture Notes in Control and Information Sciences, pp. 95–110, Springer-Verlag Limited, `http://stanford.edu/~boyd/graph_dcp.html`.

Hauksson, E., and P. Shearer (2005), Southern California hypocenter relocation with waveform cross-correlation, part 1: Results using the double-difference method, *Bulletin of the Seismological Society of America*, *95*(3), 896–903.

Hayes, G. P., P. S. Earle, H. M. Benz, D. J. Wald, and R. W. Briggs (2011), 88 Hours: The US Geological Survey national earthquake information center response to the 11 March 2011 Mw 9.0 Tohoku earthquake, *Seismological Research Letters*, *82*(4), 481–493.

Ishii, M., P. M. Shearer, H. Houston, and J. E. Vidale (2005), Extent, duration and speed of the 2004 Sumatra–Andaman earthquake imaged by the Hi-Net array, *Nature*, *435*(7044), 933–936.

Kennett, B., and E. Engdahl (1991), Traveltimes for global earthquake location and phase identification, *Geophysical Journal International*, *105*(2), 429–465.

Kiser, E., and M. Ishii (2012), Combining seismic arrays to image the high-frequency characteristics of large earthquakes, *Geophysical Journal International*, *188*(3), 1117–1128.

Kiser, E., and M. Ishii (2017), Back-projection imaging of earthquakes, *Annual Review of Earth and Planetary Sciences*, *45*, 271–299.

Krüger, F., and M. Ohrnberger (2005), Tracking the rupture of the M w= 9.3 Sumatra earthquake over 1,150 km at teleseismic distance, *Nature*, *435*(7044), 937–939.

Lay, T., H. Kanamori, C. J. Ammon, M. Nettles, S. N. Ward, R. C. Aster, S. L. Beck, S. L. Bilek, M. R. Brudzinski, R. Butler, et al. (2005), The great Sumatra-Andaman earthquake of 26 december 2004, *science*, *308*(5725), 1127–1133.

Lipa, J. E., B. M. Worthmann, and D. R. Dowling (2018), Measurement of autoproduct fields in a Lloyd's mirror environment, *The Journal of the Acoustical Society of America*, *143*(4), 2419–2427.

Liu, Z., C. Song, L. Meng, Z. Ge, Q. Huang, and Q. Wu (2017), Utilizing a 3D global P-wave tomography model to improve backprojection imaging: A case study of the 2015 Nepal earthquake, *Bulletin of the Seismological Society of America*, *107*(5), 2459–2466.

Manchee, E. B., and D. H. Weichert (1968), Epicentral uncertainties and detection probabilities from the Yellowknife seismic array data, *Bulletin of the Seismological Society of America*, *58*(5), 1359–1377.

McFadden, P., B. Drummond, and S. Kravis (1986), The N th-root stack: Theory, applications, and examples, *Geophysics*, *51*(10), 1879–1892.

Meng, L., J.-P. Ampuero, J. Stock, Z. Duputel, Y. Luo, and V. Tsai (2012a), Earthquake in a maze: Compressional rupture branching during the 2012 Mw 8.6 Sumatra earthquake, *Science*, *337*(6095), 724–726.

Meng, L., J.-P. Ampuero, Y. Luo, W. Wu, and S. Ni (2012b), Mitigating artifacts in back-projection source imaging with implications for frequency-dependent properties of the Tohoku-Oki earthquake, *Earth, planets and space*, *64*(12), 1101–1109.

Meng, L., A. Zhang, and Y. Yagi (2016), Improving back projection imaging with a novel physics-based aftershock calibration approach: A case study of the 2015 Gorkha earthquake, *Geophysical Research Letters*, *43*(2), 628–636.

550 Okuwaki, R., Y. Yagi, and S. Hirano (2014), Relationship between high-frequency radiation and asperity ruptures, revealed by hybrid back-projection with a non-planar fault model, *Scientific reports*, *4*(1), 1–6.

553 Qin, W., and H. Yao (2017), Characteristics of subevents and three-stage rupture processes of the 2015 Mw 7.8 Gorkha Nepal earthquake from multiple-array back projection, *Journal of Asian Earth Sciences*, *133*, 72–79.

556 Ricker, N. (1953), Wavelet contraction, wavelet expansion, and the control of seismic resolution, *Geophysics*, *18*(4), 769–792.

558 Rost, S., and C. Thomas (2002), ARRAY SEISMOLOGY: METHODS AND APPLICATIONS, *Reviews of Geophysics*, *40*(3), 2–1–2–27, doi:10.1029/2000RG000100, 1008.

560 Shearer, P. M. (1997), Improving local earthquake locations using the L1 norm and waveform cross correlation: Application to the Whittier Narrows, California, aftershock sequence, *Journal of Geophysical Research: Solid Earth*, *102*(B4), 8269–8283.

563 Tan, F., Z. Ge, H. Kao, and E. Nissen (2019), Validation of the 3-D phase-weighted relative back projection technique and its application to the 2016 M w 7.8 Kaikōura Earthquake, *Geophysical Journal International*, *217*(1), 375–388.

566 VanDecar, J., and R. Crosson (1990), Determination of teleseismic relative phase arrival times using multi-channel cross-correlation and least squares, *Bulletin of the Seismological Society of America*, *80*(1), 150–169.

569 Walker, K. T., and P. M. Shearer (2009), Illuminating the near-sonic rupture velocities of the intracontinental Kokoxili Mw 7.8 and Denali fault Mw 7.9 strike-slip earthquakes with global P wave back projection imaging, *Journal of Geophysical Research: Solid Earth*, *114*(B2).

572 Wang, D., and J. Mori (2011), Rupture process of the 2011 off the Pacific coast of Tohoku Earthquake (M w 9.0) as imaged with back-projection of teleseismic P-waves, *Earth, planets and space*, *63*(7), 603–607.

575 Wang, D., and J. Mori (2016), Short-period energy of the 25 April 2015 M w 7.8 Nepal earthquake determined from backprojection using four arrays in Europe, China, Japan, and Australia, *Bulletin of the Seismological Society of America*, *106*(1), 259–266.

578 Wang, D., N. Takeuchi, H. Kawakatsu, and J. Mori (2016), Estimating high frequency energy radiation of large earthquakes by image deconvolution back-projection, *Earth and Planetary Science Letters*, *449*, 155–163.

581 Wang, K., and Y. Fialko (2015), Slip model of the 2015 Mw 7.8 Gorkha (Nepal) earthquake from inversions of ALOS-2 and GPS data, *Geophysical Research Letters*, *42*(18), 7452–7458.

Worthmann, B. M., and D. R. Dowling (2017), The frequency-difference and frequency-sum acoustic-field autoproducts, *The Journal of the Acoustical Society of America*, *141*(6), 4579–4590.

Worthmann, B. M., H. Song, and D. R. Dowling (2017), Adaptive frequency-difference matched field processing for high frequency source localization in a noisy shallow ocean, *The Journal of the Acoustical Society of America*, *141*(1), 543–556.

Xu, Y., K. D. Koper, O. Sufri, L. Zhu, and A. R. Hutko (2009a), Rupture imaging of the Mw 7.9 12 May 2008 Wenchuan earthquake from back projection of teleseismic P waves, *Geochemistry, Geophysics, Geosystems*, *10*(4).

Xu, Y., K. D. Koper, O. Sufri, L. Zhu, and A. R. Hutko (2009b), Rupture imaging of the Mw 7.9 12 May 2008 Wenchuan earthquake from back projection of teleseismic P waves, *Geochemistry, Geophysics, Geosystems*, *10*(4), n/a–n/a, doi:10.1029/2008GC002335, q04006.

Yagi, Y., and R. Okuwaki (2015), Integrated seismic source model of the 2015 Gorkha, Nepal, earthquake, *Geophysical Research Letters*, *42*(15), 6229–6235.

Yin, J., M. A. Denolle, and H. Yao (2018), Spatial and temporal evolution of earthquake dynamics: case study of the Mw 8.3 Illapel Earthquake, Chile, *Journal of Geophysical Research: Solid Earth*, *123*(1), 344–367.

Yue, H., J. C. Castellanos, C. Yu, L. Meng, and Z. Zhan (2017), Localized water reverberation phases and its impact on backprojection images, *Geophysical Research Letters*, *44*(19), 9573–9580.

Zeng, H., S. Wei, and W. Wu (2020), Sources of uncertainties and artefacts in back-projection results, *Geophysical Journal International*, *220*(2), 876–891.

Zhang, H., S. Van Der Lee, and Z. Ge (2016), Multiarray rupture imaging of the devastating 2015 Gorkha, Nepal, earthquake sequence, *Geophysical Research Letters*, *43*(2), 584–591.

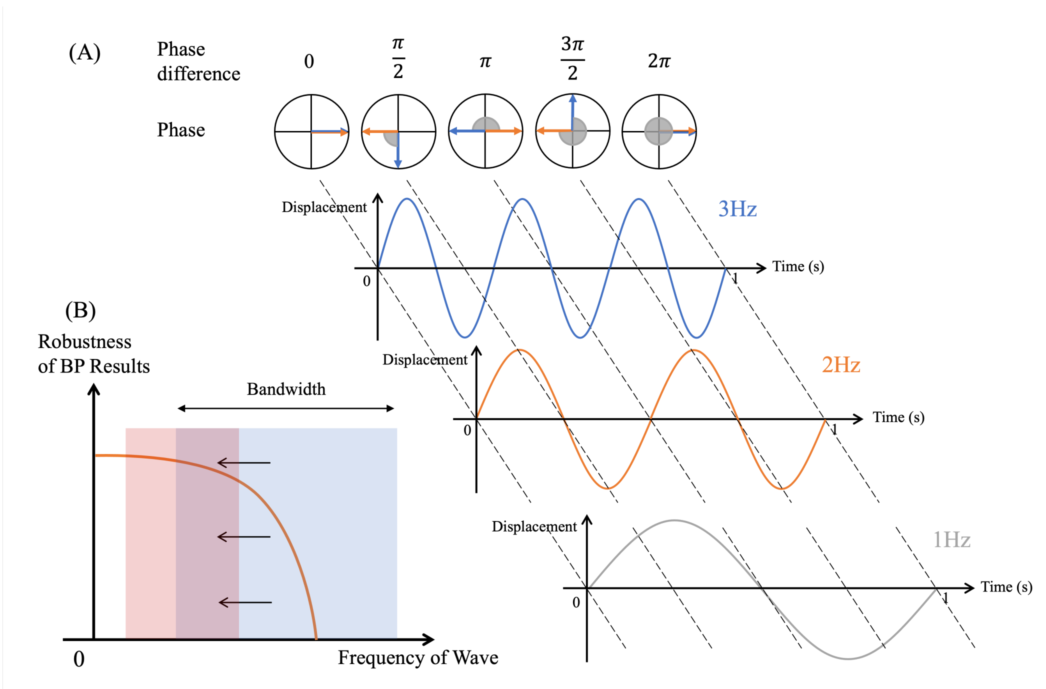

Figure 1. Conceptual sketch of FDBP. (A) Phase difference between two waves (3Hz and 2Hz) mimicking the phase of a wave at a difference frequency (1Hz). Arrows show the phase of the waves, and the angle indicates the phase difference. (B) Conceptual graph demonstrating FDBP decreases the bandwidth (extent of blue box) to a lower apparent bandwidth (extent of red box), increasing the robustness of the results.

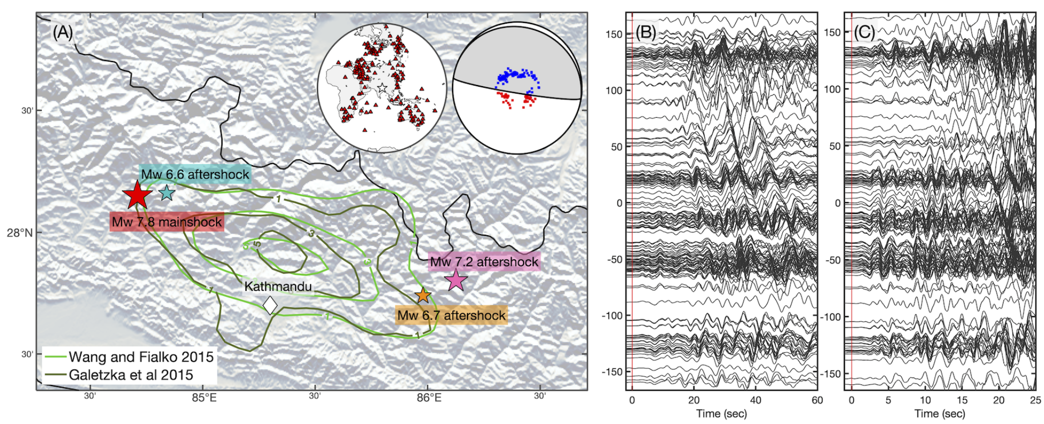

Figure 2. The 2015 M 7.8 Gorkha Nepal earthquake and its waveforms. (A) Map view of the source region and its three large aftershocks. Contours show finite-fault slip models of *Wang and Fialko* [2015] and *Galetzka et al.* [2015] (1:2:6 meters contours). Insets show the stations used in this study and the mainshock focal mechanism. (B) Low frequency (0.05–0.5 Hz) waveforms, first 60 s. (C) High frequency (0.3-2Hz) waveforms, first 25 s. The waveforms are self-normalized by the first 15 s and arranged by the station azimuth (vertical-axis).

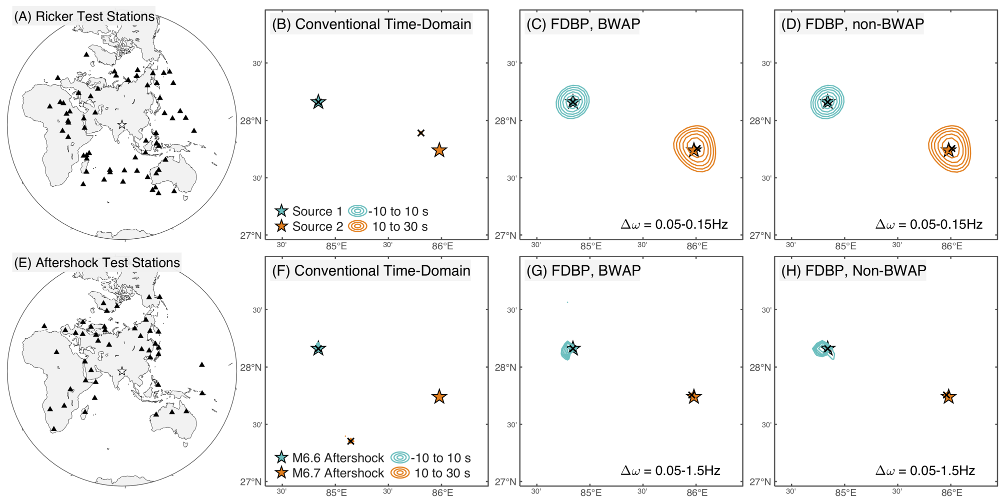

Figure 3. Synthetic tests. (A) Station distribution of the Ricker test, map view with Lambert azimuthal equal-area projection. The white star shows the location of the two sources. (B-D) Backprojection results of CTBP, BWAP, and non-BWAP. The difference-frequencies used for BWAP and non-BWAP is 0.05-0.15 Hz. The time windows are 20 s long each. The backprojection results are plotted with contours of 80:4:100. Black crosses indicate the location of the backprojection peak loci. (E–H) are similar to (A–D), but for the aftershock composite "synthetic" waveform test and difference-frequencies of 0.05-1.5 Hz.

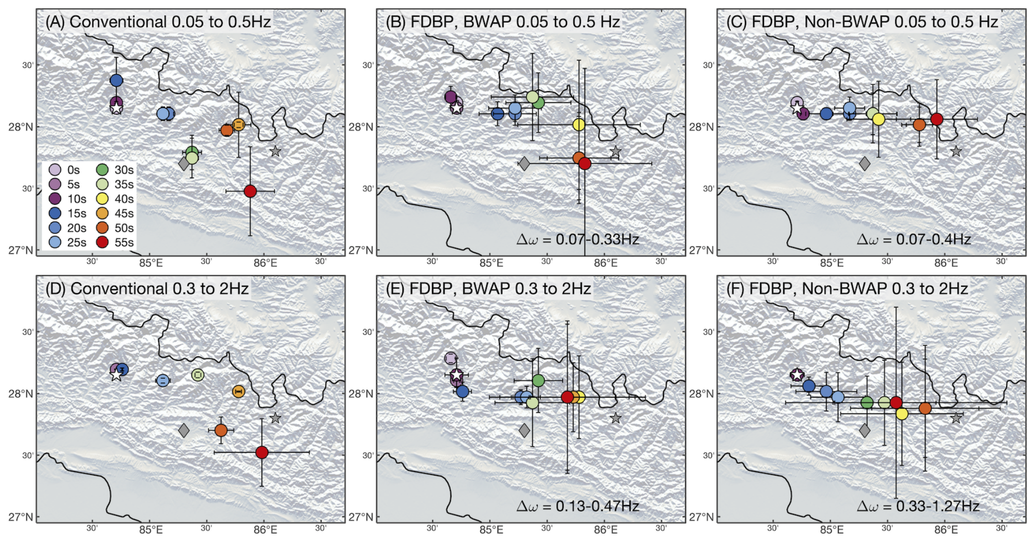

Figure 4. Backprojection results of the 2015 Gorkha, Nepal mainshock. The three columns show results of CTBP, BWAP, and non-BWAP. The top row shows the low frequency (0.05–0.5 Hz) radiation results. The bottom row shows the high frequency (0.3–2 Hz) radiation results. The centroid time of each time window is indicated in the legend. The standard errors of the peak loci is shown as the error bars. The white star, grey diamond, and grey star indicate the mainshock, Kathmandu, and the M7.3 aftershock, respectively.

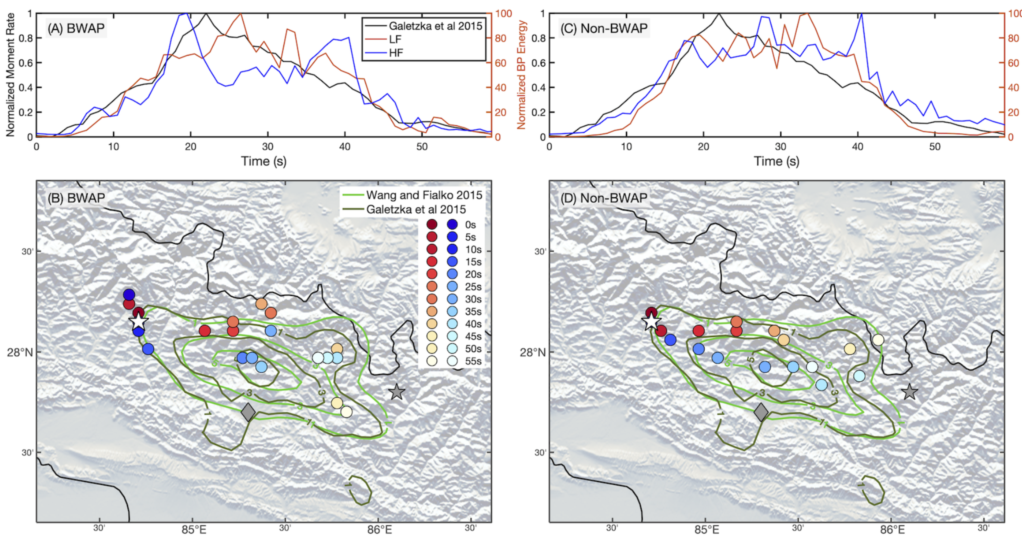

Figure 5. Comparison of the FDBP results with finite-fault slip models. (A) Normalized FDBP BWAP peak power time functions and moment-rate function in *Galetzka et al.* [2015]. (B) FDBP BWAP results and finite-fault slip models [*Wang and Fialko*, 2015; *Galetzka et al.*, 2015]. The LF and HF FDBP results are shown as red and blue circles respectively. The centroid time of each time window is indicated in the legend. The finite-fault slip models [*Wang and Fialko*, 2015; *Galetzka et al.*, 2015] are shown with contours of 1:2:6 meters. The white star, grey diamond, and grey star are the mainshock, Kathmandu, and the M7.3 aftershock, respectively. (C–D) similar to (A–B), but for the FDBP non-BWAP results.

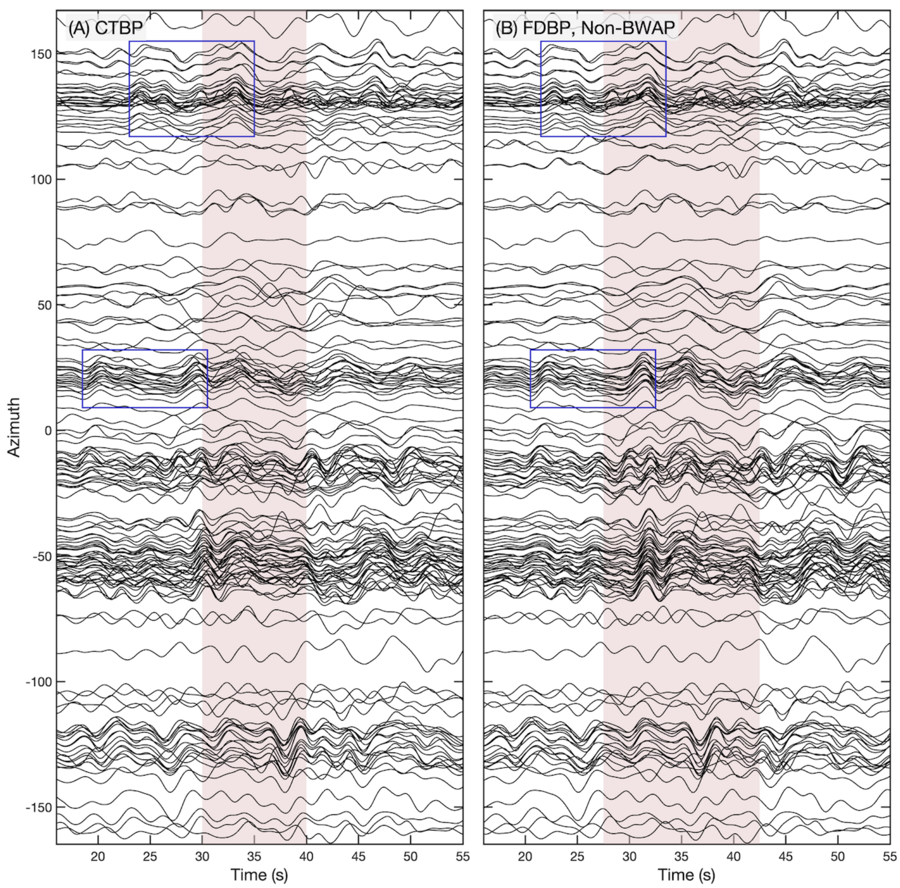

Figure 6. LF waveforms realigned at time window 8 (centered at 35 s). The alignments are based on the peak loci of the (A) CTBP and (B) FDBP Non-BWAP results. Time window 8 is delineated by the red patch in the background and the waveforms are self-normalized by their first 35 s. Blue boxes highlight similar sets of pulses for visual comparisons.